

1 Size-differentiated Export in Different Dynamical 2 Regimes in the Ocean

3 **M. Dever¹, D. Nicholson¹, M. M. Omand², and A. Mahadevan¹**

4 ¹Woods Hole Oceanographic Institution, Woods Hole, MA 02543, USA

5 ²Graduate School of Oceanography, University of Rhode Island, Narragansett, Rhode Island, USA

6 **Key Points:**

- 7 Submesoscale dynamics enhance the contribution of slow-sinking particles to
8 POC export, especially for steep particle size-spectrum slopes
- 9 Remineralization processes intensify the role of slow-sinking particles, to the
10 point where these particle sometime dominate POC export

11 **Abstract**

12 Export of Particulate Organic Carbon (POC) is mainly driven by gravitational sinking.
 13 Thus, traditionally, it is thought that larger, faster-sinking particles make up most of
 14 the POC export flux. However, this need not be the case in a dynamic oceanic flow
 15 field, where the ocean velocity can influence the descent rate of particles. Particles
 16 with different settling speeds are released in two process-oriented model simulations
 17 of an upper ocean eddying flow to evaluate the impact of (1) ocean dynamics on the
 18 respective contribution of the different sinking-velocity classes to POC export, and (2)
 19 the particle number size-spectrum slope. The analysis reveals that the leading export
 20 mechanism changes from gravitationally-driven to advectively-driven as submesoscale
 21 dynamics become more important. The vertical velocity associated with submesoscale
 22 dynamics enhances the contribution of slower-sinking particles to POC export^{c1}, es-
 23 pecially where the relative abundance of small particles is larger, as captured by a
 24 steeper particle size-spectrum slope. ^{c2}Remineralization ^{c3} generally decreases the
 25 total amount of biomass exported, but its impact is weaker in dynamical regimes where
 26 submesoscale dynamics are present and export is advectively-driven. ^{c4}In an advec-
 27 tively-driven export regime, remineralization processes counter-intuitively enhance the
 28 role of slower-sinking particles to the point where these slower-sinking velocity classes
 29 dominate the export, therefore challenging the traditional paradigm for POC export.
 30 This study demonstrates that slow-sinking particles can be a significant contribution,
 31 and at times, even dominate the export flux.

32 **1 Introduction**

33 Photosynthesis in the sunlit upper ocean and the production of Particulate Or-
 34 ganic Carbon (POC) takes up dissolved inorganic carbon and facilitates the uptake
 35 of CO₂ from the atmosphere. The sinking of POC exports organic carbon from the
 36 upper ocean to the interior, leading to the sequestration of carbon (Falkowski, Barber,
 37 & Smetacek, 1998) on timescales ranging from days to years depending on the sink-
 38 ing depth and circulation. Understanding the mechanisms driving the export of POC
 39 from the ocean's surface to the interior is therefore crucial to better constrain Earth's
 40 carbon budget.

41 Traditionally, POC export is thought to occur through gravitational sinking and
 42 one-dimensional models have been used to describe the sinking POC flux with depth.
 43 Particles produced through primary and secondary production in the surface layer
 44 that are relatively large and fast-sinking, tend to sink out of the upper surface layer
 45 on timescales shorter than the timescale on which the particles get remineralized.
 46 It is reasonable to treat POC export as sinking-dominated if the vertical advective
 47 velocities in the ocean are weaker than the velocities associated with gravitational
 48 sinking. However, Particulate Organic Matter (POM) has a wide range of particle
 49 shape, size and type, that result in particle sinking velocities ranging from practically
 50 zero, to several hundreds of meters per day. The size spectrum, or number distribution
 51 of particle sizes, is usually characterized by a power law with the power ranging between
 52 -2 and -4, for which the abundance of small particles is $\mathcal{O}(10^4 - 10^8)$ greater than large
 53 particles. The biomass size spectrum, which indicates the distribution of biomass vs.
 54 particle size, tends to be flatter and variable in shape (Sheldon, Prakash, & Sutcliffe,
 55 1972) compared to the particle number spectrum, because the volume (and mass) of

^{c1} A steeper particle size spectrum, also increases the relative contribution of smaller, slower-sinking particles

^{c2} Implementing a r

^{c3} scheme

^{c4} Under specific conditions

a particle scales with its linear size raised to a power that exceeds 1 (and typically varies between 2 and 3 depending on shape and porosity). Importantly, it means that a significant fraction of the particulate biomass is in the small size fraction. Even though the sinking velocity w_s of particles does not perfectly relate to particle size l , it is fair to assume that $w_s \sim l^n$ (with $n = 2$ according to Stokes law, and $1 < n < 2$ for complex particle shapes). Due to this, as well as the fact that particles of organic matter are not very much greater in their densities than seawater, a significant fraction of the biomass sinks very slowly (at velocities less than tens of meters per day). When the gravitational sinking velocity of particles is comparable to (or smaller than) the vertical velocities in the flow field, the dynamics of the flow field can impact the trajectories and fate of the POC. Thus, depending on the flow dynamics, and the fraction of slow-sinking particulate biomass, the sinking of organic matter can be affected by the fluid flow in the ocean.

Recent studies have shown that ocean dynamics can play a role in driving the transport of carbon from the euphotic layer to the ocean interior. For example, enhanced vertical velocities along the edge of a mesoscale eddy led to a funneling of particles along the eddy's periphery (van Haren, Millot, & Taupier-Letage, 2006; Waite et al., 2016). Omand et al. (2015) found that submesoscale mixed layer eddies, while contributing to the restratification of a frontal zone, were subducting a large amount of non-sinking POC from the surface productive layer during the onset of the Spring bloom in the subpolar North Atlantic. Advectively subducting plumes or filaments of high oxygen, chlorophyll and small POC (evidenced through backscatter) were detected from a suite of gliders during the North Atlantic Bloom experiment (Alkire et al., 2012). Using model simulations to capture the process of eddy-driven subduction, Omand et al. (2015) estimated the downward advective flux of non-sinking POC and parameterized it. Briggs et al. (2011) quantified the flux of fast-sinking particles consisting largely of diatoms from observations of optical backscatter. But, these estimates did not account for a range of sinking particle velocities. Typically, particulate organic matter (POM) has a wide spectrum of sinking velocities and in order to understand its fate and export, we need to consider the biomass distribution as a function of the particle sinking velocity spectrum and its interaction with the dynamics of the flow field in the ocean.

A growing body of literature focusing on submesoscale (1-10 km) dynamics is exploring its impact on biogeochemical processes (Lévy, Ferrari, Franks, Martin, & Rivière, 2012; Mahadevan, 2016). Submesoscale dynamics, characterized by Rossby numbers of order 1, typically develop in filaments in areas where sharp density fronts exist (Klein & Lapeyre, 2009; McWilliams, 2016; Thomas, Taylor, Ferrari, & Joyce, 2013). In this dynamical regime, geostrophic balance breaks down and a secondary ageostrophic circulation develops across the front, capable of generating large vertical velocities on the order of 100 m/day (Fox-Kemper, Ferrari, & Hallberg, 2008; Mahadevan, 2016). On the denser side of the front, the vorticity is cyclonic and associated with downwelling velocities, while anticyclonic vorticity and upwelling is expected on the lighter side of the front. The distribution of relative vorticity across a front is asymmetric and skewed toward cyclonic vorticity (Rudnick, 2001), leading to more localized and more intense downwelling regions, as opposed to weaker and larger upwelling regions (Mahadevan & Tandon, 2006). Enhanced vertical velocities can generate a local bloom by supplying nutrients to the sunlit layer of the ocean (Lévy, Klein, & Treguier, 2001; Mahadevan & Archer, 2000), or can significantly increase the export of POC to the ocean interior through downwelling (Estapa et al., 2015; Gruber et al., 2011; Lévy et al., 2012; Omand et al., 2015).

The downwelling velocities $\mathcal{O}(100 \text{ m/day})$ generated at submeso-scales provide a physical mechanism capable of competing with gravitational sinking and thus exporting particles over a larger portion of the particle size spectrum. Through this

109 mechanism, smaller particles can be exported on timescales shorter than their rem-
 110 ineralization timescales, despite their slower sinking velocities. Depending on the frac-
 111 tion of biomass in smaller particles (i.e., with slow sinking velocities), the impact of
 112 submesoscale dynamics on the export of POC is potentially significant.

113 In this study, we account for a range of particle sinking velocities in a dynamic
 114 flow field. Despite progress on sampling and viewing particles in the ocean (McDonnell
 115 & Buesseler, 2010), direct measurements of particles sinking velocities are difficult
 116 to obtain, and often inferred from key parameters such as particle type, size, and
 117 density. Though we acknowledge a large variability in these relationships, we assume
 118 a relationship between particle size, biomass, and particle sinking velocity in order to
 119 assess the impact of the flow dynamics and particle size spectrum on the export flux.

120 We rely on a submesoscale-resolving, non-hydrostatic ocean model to simulate the
 121 dynamics in the upper few hundred meters of the ocean. The model does not represent
 122 surface waves or boundary layer turbulence, but rather, examines the fate of particulate
 123 organic matter beneath the turbulent surface boundary layer. The dynamical model
 124 is coupled with a particle-tracking module to model the advection of particles by fluid
 125 flow, while neglecting the effects of particle inertia and drag on their advection. In
 126 addition, the particles sink with a range of sinking velocities (between 0.025–5 m
 127 day⁻¹).

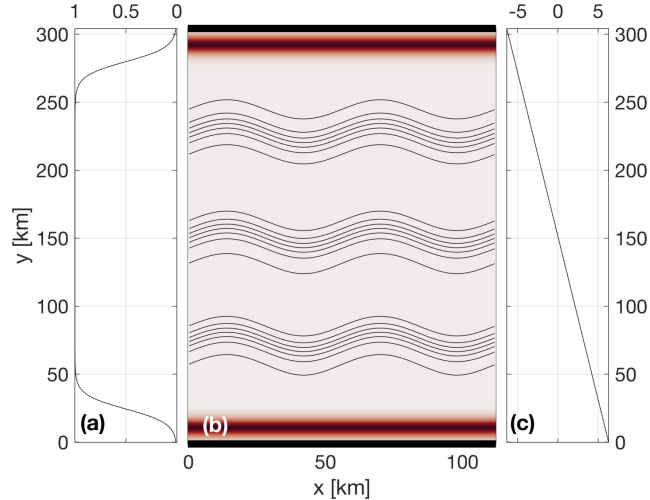
128 The model is used to quantify the contribution of slow-sinking particles to carbon
 129 export, as a function of (1) the dynamics of the flow field, (2) the slope of the sinking
 130 velocity spectrum, and (3) the remineralization timescale. Particles in the model
 131 are prescribed with both a constant and time-varying sinking velocity to mimic a
 132 remineralizing behavior. Particles are released in two fundamentally different flow
 133 fields in terms of dynamics based on observed conditions in the Northeast Pacific:
 134 In the summer, where ocean dynamics are characterized by low Rossby numbers and
 135 weak vertical advective velocities, and in the winter, where ocean dynamics include
 136 submesoscale frontal structures and local Rossby numbers $\mathcal{O}(1)$. Both simulations
 137 and the particle-tracking module are described in Section 2. The impact of particles
 138 characteristics and ocean dynamics on the export of POC is quantified in Section 3,
 139 and discussed in Section 4. Section 5 summarizes the key conclusions of the study.

140 2 Methods

141 2.1 Model setup and domain

142 This study uses a non-hydrostatic, three-dimensional, Process Study Ocean Model
 143 (PSOM; Mahadevan, Olinger, & Street, 1996a, 1996b) to simulate an eddy field that is
 144 representative of the Northeast Pacific Ocean. The model is set in a channel configura-
 145 tion with periodic east-west boundaries, and solid boundaries in the south and north.
 146 The domain covers 112 km in the x-direction, 304 km in the y-direction, and 1000 m
 147 in the vertical (Figure 1). The horizontal resolution is 500 m, while a stretched grid is
 148 used in the vertical with 32 levels ranging in thickness from 1.25 m near the surface to
 149 70 m at the lowermost level. The model is integrated numerically in time and evolves
 150 the temperature, salinity, free-surface height, pressure, and three-dimensional velocity
 151 field from an initial state, subject to momentum and buoyancy fluxes applied through
 152 the surface boundary.

160 Time-varying wind stress and heat flux are prescribed at the surface boundary.
 161 Time series are computed from measurements collected at Station Papa and available
 162 through the Pacific Marine Environmental Laboratory (PMEL, 2018). Daily wind
 163 stress and net heat fluxes are calculated over the period 2007–2016 to produce a year-
 164 long climatology. A squared low-pass filter with a cut-off frequency of 8.5 days is
 165 applied to both time series to remove high-frequency variability. In all numerical



153 **Figure 1.** PSOM model setup. (a) Meridional profile of scaling coefficient that multiplies the
 154 time-varying zonal wind stress τ_x shown in Fig. 3a. The taper at north and south boundaries
 155 prevents ‘coastal’ up-/down-welling being entirely concentrated in the boundary grid cell. (b)
 156 Restoration factor (color shading) used to dampen internal wave reflection at boundaries as well
 157 as up-/down-welling due to the windstress curl. Surface density contours (black) show the three
 158 fronts used to initialize the model. (c) Meridional variation of the time-dependent surface heat
 159 flux (Fig. 3a) prescribed over the domain.

166 experiments, simulations are run for the first 5 days without any forcing applied to
 167 the surface boundary. Surface wind stress and heat fluxes are then linearly ramped up
 168 between days 5 and 10 of the simulation, to reach realistic values at day 10.

169 While the meridional component, τ_y , is set to zero, the zonal component of
 170 the wind stress, τ_x , is prescribed at the surface throughout the model domain and
 171 is tapered at the northern and southern boundaries to avoid excessive Ekman-driven
 172 upwelling and downwelling (Figure 1a). A restoration timescale is prescribed to contain
 173 the curl-driven upwelling and downwelling regions generated by the tapering of the
 174 wind stress, as well as to limit internal wave reflection at the solid boundaries back
 175 into the domain (Figure 1b). While net surface heat fluxes are homogeneous in the
 176 zonal direction, a meridional gradient is maintained throughout the simulation. The
 177 meridional gradient was determined from the North American Regional Reanalysis
 178 (NARR) product (Mesinger et al., 2006), and set to $1/24 \text{ W/m}^2/\text{km}$ (Figure 1c).

179 Initial hydrographic conditions are determined from a three-dimensional gridded
 180 field of temperature and salinity from Argo floats (Gaillard, 2015; Gaillard, Reynaud,
 181 Thierry, Kolodziejczyk, & von Schuckmann, 2016). Argo data is averaged monthly
 182 over the period 2002-2012 and two different months are used to initialize the two main
 183 numerical experiments for this study: Climatological conditions in April are used to
 184 initialize the *Papa-summer* experiment, while January climatological conditions are
 185 used to initialize the *Papa-winter* experiment (Table 1). The north-south background
 186 density gradient is then intensified into three fronts located at $y = 75$, $y = 150$, and
 187 $y = 225 \text{ km}$ (Figure 1). The amplitude of the density gradient associated with the three
 188 fronts is determined from the probability distribution function (PDF) of the density
 189 gradients measured by underwater gliders deployed around Station Papa over the
 190 period 2008-2010 (Pelland, 2018; Pelland, Eriksen, & Cronin, 2016). To reduce model
 191 spin-up time, density fronts are perturbed by a sinusoidal wave with a wavelength close

220 **Table 1.** Summary of the key characteristics of PSOM experiments *Papa-summer* and
 221 *Papa-winter*.

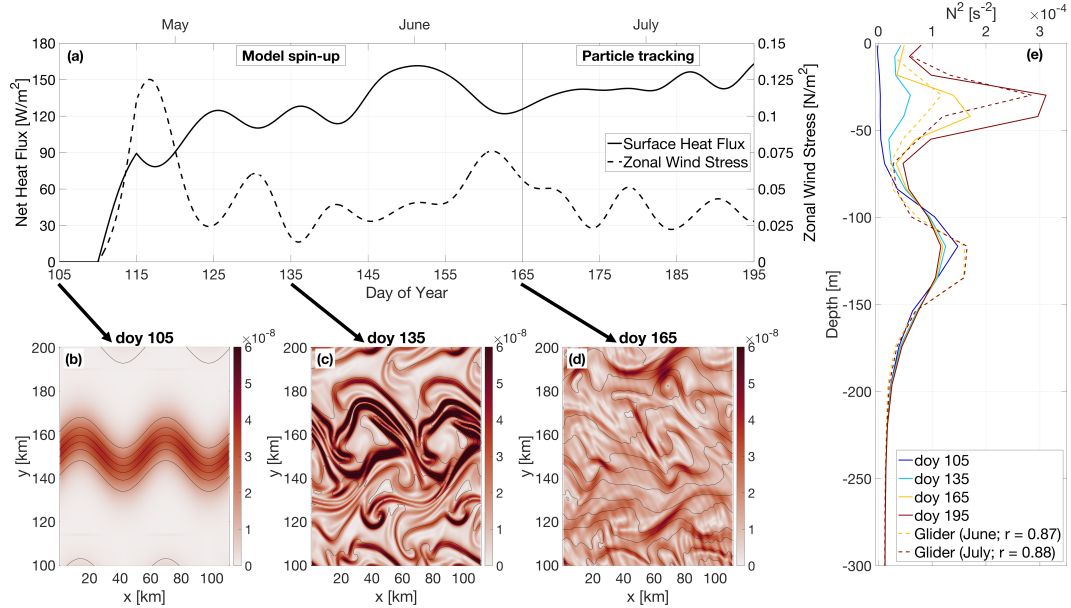
	<i>Papa-summer</i>	<i>Papa-winter</i>
Time period	April – July	January – March
Spin-up	60 days	50 days
Advective timestep	216 s	108 s
Horizontal diffusivity	1 m ² s ⁻¹	0.2 m ² s ⁻¹
Restoration timescale	3 days	15 days
Zonal wind stress	0 – +0.16 N m ⁻²	-0.05 – +0.17 N m ⁻²
Surface heat flux	-46.8 – +167.5 W m ⁻²	-57.6 – +15.3 W m ⁻²
Maximum M ² ($\times 10^{-8}$)		
initial	3.2 s ⁻²	33.9 s ⁻²
spun-up	12.0 s ⁻²	50.0 s ⁻²
Maximum N ² ($\times 10^{-4}$)		
initial	1.5 s ⁻²	1.6 s ⁻²
spun-up	3.1 s ⁻²	1.1 s ⁻²
Averaged mixed layer depth		
initial	73 m	85 m
spun-up	11 m	93 m

192 to the 1st baroclinic deformation radius ($\lambda = 66$ km). Similar PSOM configurations
 193 were successfully used in previous studies (Mahadevan, D’Asaro, Lee, & Perry, 2012;
 194 Omand et al., 2015).

195 Two main experiments are conducted using the same configuration of PSOM,
 196 where only initial conditions and surface forcings are varied: *Papa-summer* aims
 197 at generating ocean dynamics representing conditions in the Northeast Pacific in
 198 the summertime. Summer ocean dynamics are characterized by a flow generally in
 199 geostrophic balance, with relatively weak density gradients and low Rossby numbers
 200 ($\ll 1$). *Papa-winter* aims at capturing wintertime ocean conditions in the region. A
 201 different dynamical regime is expected to dominate during wintertime when mixed
 202 layers are deeper and lateral density gradients enhanced, with sharper density fronts,
 203 filament-like features and localized Rossby number $\mathcal{O}(1)$ over spatial scales $\mathcal{O}(1$ km)
 204 (Callies, Ferrari, Klymak, & Gula, 2015; Mensa et al., 2013; Thompson et al., 2016).
 205 The individual characteristics of each of
 206 *Papa-summer* and *Papa-winter* are detailed below.

207 2.1.1 *Papa-summer* Model Experiment

208 In *Papa-summer*, PSOM is initialized based on climatological Argo data in April.
 209 The magnitude of the density gradient across the front is set to 3.34×10^{-6} kg/m³/m,
 210 which corresponds to the 95th percentile of the PDF of density gradients measured
 211 in April from glider data collected in the region (Figure 2 and Table 1). The model
 212 is run with a timestep of 216 s and is allowed to spin-up for 60 days, allowing sum-
 213 mer stratification to develop. The model is then run for 30 additional days, saving
 214 instantaneous model fields every 3 hours for particle tracking. The month of April
 215 is chosen for initialization so the experiment would capture the onset of positive net
 216 heat fluxes, and the summer restratification that ensues in July-August (Figure 2). In
 217 this region, the summer stratification is associated with large primary productivity,
 218 particle production, and POC export (e.g., fecal pellets, dead phytoplankton; Plant
 219 et al., 2016).



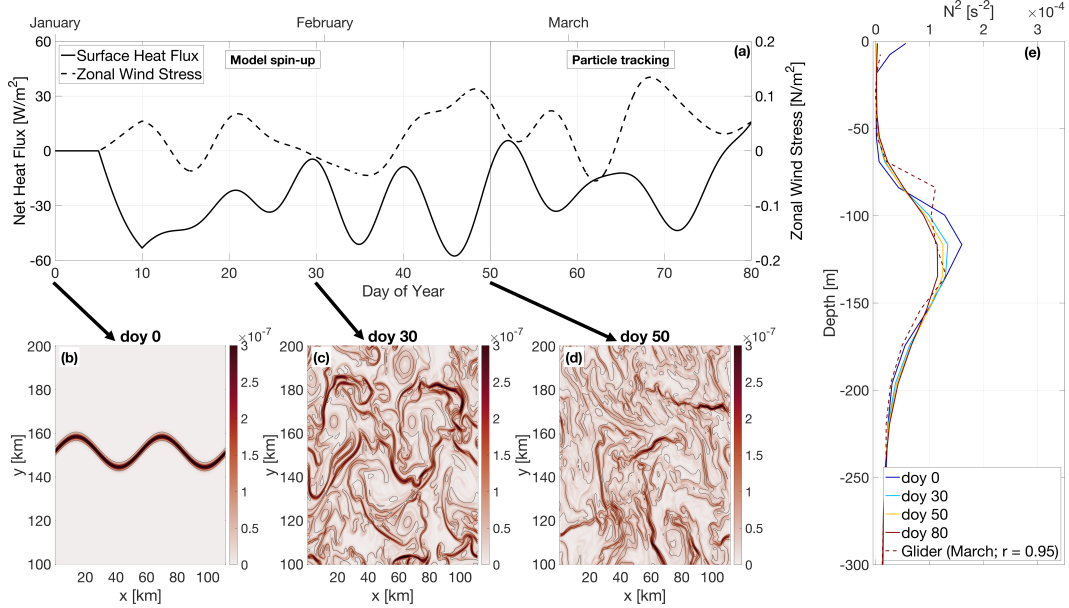
222 **Figure 2.** PSOM configuration for *Papa_summer*. (a) Time series of net heat fluxes and wind
 223 stress prescribed at the surface. Notice the positive heat fluxes, as well as downfront winds (i.e.
 224 eastward) persisting throughout the experiment. (b)-(d) surface horizontal buoyancy gradients
 225 $M^2 = |\nabla_H b|^2$ (in s^{-2}) at day of year (doy) 105, 135, and 165. Black contours show isopycnals (in
 226 kg/m³; CI = 0.01 kg/m³). (e) Vertical profile of the buoyancy frequency N^2 at day of year 105,
 227 135, 165, and 195, showing the development of summer stratification centered at $z = 30$ m (solid
 228 lines). Monthly-average vertical stratification obtained from glider profiles collected in June and
 229 July are superimposed (dashed lines), along with the correlation coefficient between observations
 230 and model outputs.

2.1.2 *Papa_winter Model Experiment*

231 In *Papa_winter*, PSOM is initialized based on climatological Argo data in January.
 232 The frontal gradient is set to 3.54×10^{-5} kg/m³/m, which corresponds to the
 233 99th percentile of the PDF of density gradients measured in January from glider data
 234 collected in the region (Figure 3 and Table 1). The model is allowed to spin-up for 50
 235 days allowing for the prescribed fronts to become unstable. To accommodate for the
 236 larger density gradients and stronger velocities, the advective timestep is shortened to
 237 108 s and the horizontal diffusivity is lowered to 0.2 m²/s throughout the experiment.
 238 The model is run for 30 additional days, saving instantaneous model fields every 1.5
 239 hours for particle tracking. The month of January is chosen for initialization so the
 240 experiment would capture the time of year where the mixed layer is the deepest, and
 241 Rossby number O(1) occur more frequently. The objective is for this experiment to
 242 contrast *Papa_summer* by capturing the statistics of ocean conditions dominated by
 243 submesoscale dynamics.

2.1.3 *Validation*

244 To ensure that PSOM simulations yielded realistic conditions for both *Papa_summer*
 245 and *Papa_winter*, distributions of horizontal (M^2) and vertical (N^2) buoyancy gradi-
 246 ents are compared with glider observations collected over the period 2008-2009 (Pelland
 247 et al., 2016). During this period, underwater gliders sampled in a “bow-tie” pattern



245 **Figure 3.** PSOM configuration for *Papa_winter*. (a) time series of net heat fluxes and wind
 246 stress prescribed at the surface. Notice the mostly negative heat fluxes, as well as alternating
 247 zonal wind direction. (b)-(d) surface horizontal buoyancy gradients $M^2 = |\nabla_H b|^2$ (in s^{-2}) at day
 248 of year (doy) 0, 30, and 50. Black contours show isopycnals (in kg/m^3 ; CI = $0.01 kg/m^3$). (e)
 249 Vertical profile of the buoyancy frequency N^2 at doy 0, 30, 50, and 80, showing the persistence
 250 of the halocline between $z = 80$ and $z = 180$ m throughout the experiment (solid lines). Monthly-
 251 average vertical stratification obtained from glider profiles collected in March is superimposed
 252 (dashed line), along with the correlation coefficient between observations and model outputs.
 253

258 centered on Station Papa. Gliders sample the water column in a triangular wave
 259 pattern, whose shape is easily affected by currents, due to the slow moving speed of
 260 the glider (~ 1 km/hr). It is therefore challenging to associate a specific spatial scale
 261 with gradients computed between glider profiles, as profile separation distances can be
 262 highly variable through depth and time. To circumvent this issue, horizontal buoy-
 263 ancy gradients are computed between each pair of glider profiles available within one
 264 branch of the bow-tie. Each along-track lateral buoyancy gradient is thus associated
 265 with a specific separation scale and a timestamp. Glider-based density gradients can
 266 be affected by internal waves. To filter the impact of internal waves on the PDF of
 267 horizontal buoyancy gradients, only gradients computed at a scale of twice the Rossby
 268 radius ± 1 km are considered. Rossby radii are estimated from the glider data and
 269 are ~ 8 km in winter and ~ 20 km in summer.

270 2.2 Particle Tracking Experiments

271 2.2.1 Particle Advection Scheme

To quantify the impact of submesoscale dynamics on the export of Particulate Organic Matter (POC), Lagrangian particle trajectories are computed using the same scheme as in “TRACMASS” (Döös, Kjellsson, & Jönsson, 2013) with the flow fields from the two experiments described above. The three-dimensional, non-divergent velocity components from the faces of each “C” grid cell are linearly interpolated onto the particle’s position within the grid cell. For example, the eastward (along the x-axis)

velocity of a particle is given by

$$u(x) = u_{i-1} + \frac{(x - x_{i-1})}{(x_i - x_{i-1})}(u_i - u_{i-1}), \quad (1)$$

where the subscripts $i - 1$ and i denote the western and eastern walls of the grid cell where the particle is located, respectively. This can be re-written as

$$\frac{\partial x}{\partial t} + \beta x + \delta = 0, \quad (2)$$

where $\beta = (u_i - u_{i-1})/\Delta x$ and $\delta = -u_{i-1} - \beta x_{i-1}$ (Döös et al., 2013). This differential equation can be solved analytically for $\beta \neq 0$ as

$$x_{t_1} = \left(x_0 + \frac{\delta}{\beta} \right) \exp^{-\beta(t_1 - t_0)} - \frac{\delta}{\beta} \quad (3)$$

The time it will take for the particle to reach the eastern or western face of the grid cell can be computed by taking $x_{t_1} = x_i$ or $x_{t_1} = x_{i-1}$, respectively, and solving for t_1 . For each advective timestep, the times required for the particle to reach any of the 6 walls of the grid cell are computed using (3). If any of those times is shorter than the advective timestep, the particle is advected until it reaches the cell wall. Then the flow field in the adjacent grid cell is considered and the particle is advected over the remaining time.

2.2.2 Particle Seeding

For all particle-tracking experiments, a single particle seeding event is prescribed. In the horizontal, particles are seeded every 250 m over the entire domain in the x-direction, and for $100 < y < 200$ km in the y-direction. The seeding is centered over the mean position of the central front (see Figure 2) and is therefore not affected by undesired effects created by the solid north-south solid boundaries. In the vertical, particles are seeded every 1 m between 75 and 85 m. This depth range is chosen as it corresponds to the average euphotic depth at Station Papa, defined by the 1% light level. ^{c1}Particle seeding is located at the base of the euphotic layer where biological processes not captured by the particles (e.g., grazing, repackaging, aggregation, etc.) are not as active (Ducklow, Steinberg, & Buesseler, 2001). The euphotic depth was computed for the months of February and June over the period 2007-2016 from profiles of Photosynthetically ^{c2}Active Radiation (PAR) collected at Station Papa as part of the long-term monitoring of Line P executed by the Department of Fisheries and Ocean Canada^{c2}. The average euphotic depth computed for both of these months is around 80 m, which agrees with previously established estimates of the euphotic depth (Harrison, Whitney, Tsuda, Saito, & Tadokoro, 2004; Sherry, Boyd, Sugimoto, & Harrison, 1999).

In each particle-tracking experiment, four different classes of particles are released. Each particle class is characterized by a different sinking velocity: 0.025, ^{c3}1, and 5 m/day. The slowest-sinking class is essentially selected to represent non-sinking particles: based on the setup of our experiments, the slowest-sinking particles would take 800 days on average to be exported to a depth of 100 m through gravitational sinking, a timescale much greater than commonly observed remineralization timescales. The fastest-sinking velocity is chosen as an end-member velocity class of particle that will be exported in its entirety over the course of our experiment.

^{c1} *Text added.*

^{c2} *Available*

^{c2} <https://www.waterproperties.ca/linep/index.php>

^{c3} *0.05,*

The advective timestep for particles is set to 1.5 hours. The flow field is linearly interpolated in time between model outputs, justifying the higher temporal resolution used for particle tracking in *Papa_winter*. Particle positions are saved every 3 hours, along with key model variables interpolated onto the particle positions (e.g., density, vorticity). Particles are tracked for ^{c4}four weeks (28 days). Each particle-tracking experiment contains 1,971,717 particles per sinking-velocity class, for a total of 9,858,585 particles. Particles located deeper than the maximum winter mixed layer (i.e., 100 m; Pelland et al., 2016; Plant et al., 2016) are considered exported, as they will likely not be re-entrained into the mixed layer.

2.2.3 Density and Biomass Spectra

The slope ξ of the size spectrum of particles (also known as the Junge slope; White et al., 2015) is the slope of the log-log curve of particle number N vs. particle radius r , where

$$N(r) = N_0 \left(\frac{r}{r_0} \right)^{-\xi}. \quad (4)$$

Here, N_0 and r_0 represent a reference particle number and radius, chosen arbitrarily. For small particles ($<400 \mu\text{m}$) and relatively low temperature ($<15^\circ\text{C}$), it has been shown that the relationship between particle radius r and sinking velocity w_s exhibits a range of variation and is difficult to determine empirically. Nevertheless, Stokes' law, where $w_s \propto r^2$, is often used as a lower-bound sinking velocity estimate (Bach et al., 2012).

Assuming a Stokes-like relationship, we can construct a particle sinking velocity spectrum $N(w_s)$ based on (4), as

$$N(w_s) = N_0 \left(\frac{w_s}{w_{s0}} \right)^{-\xi/2}, \quad (5)$$

where w_{s0} is the sinking speed of particles with radius r_0 . For a specific slope and sinking-velocity class, an equivalent number of particles per simulated particle can be computed using (5) (See Figure 4). For example, using the largest sinking velocity class as a reference (i.e., $w_{s0} = 5 \text{ m/day}$ and $N_0 = 1,971,717$), and a spectral slope $\xi = 4$, each simulated particle with a sinking velocity of 0.025 m/day in fact represents 40,000 particles (Figure 4). The relative biomass of a particle in a specific sinking-velocity class, $B_p(w_s)$ can be estimated if the biomass is assumed to scale with the particle's volume. The relative biomass of one particle in a sinking-velocity class w_s can therefore be computed as

$$B_p(w_s) = B_p(w_{s0}) \left(\frac{w_s}{w_{s0}} \right)^{3/2} \quad (6)$$

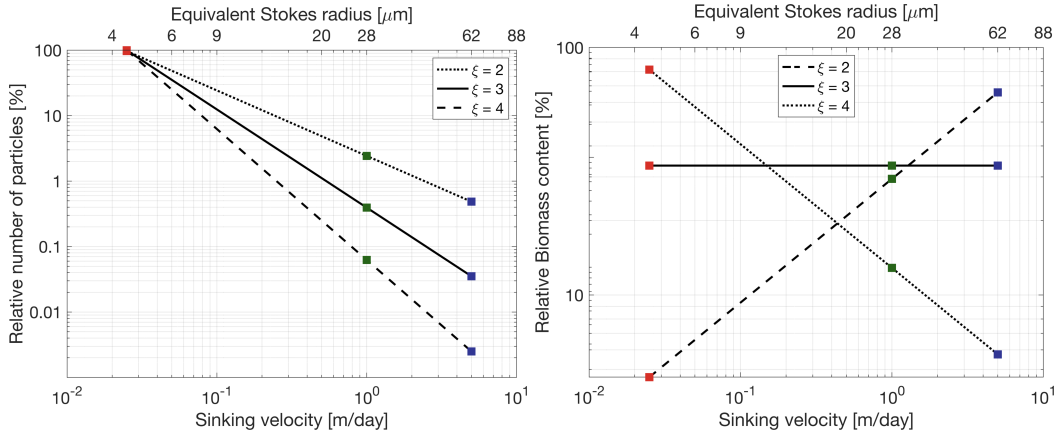
where $B_p(w_{s0})$ is the biomass of a particle in the sinking velocity class w_{s0} . The total biomass associated with one simulated particle can be obtained by scaling (6) by the ratio $N(w_s)/N_0$:

$$B(w_s) = B_0 \left(\frac{w_s}{w_{s0}} \right)^{3/2} \frac{N(w_s)}{N_0} \quad (7)$$

where $B_0 = B_p(w_{s0})$. Combining (5) and (7) yields an expression relating the biomass associated with a simulated particle for a specific sinking-velocity class and the spectral slope (Figure 4):

$$B(w_s) = B_0 \left(\frac{w_s}{w_{s0}} \right)^{\frac{3-\xi}{2}}. \quad (8)$$

^{c4} three



321 **Figure 4.** Relative number of particles (left) and biomass (right) as a function of sinking
 322 velocity w_s . Sinking velocity spectrum are shown for three different Junge slope ξ : 2 (dotted),
 323 3 (solid), and 2 (dashed). Colored squares indicate the sinking velocities of the three particle
 324 classes modeled: 0.025 m/day (red), 1 m/day (green), and 5 m/day (blue).

325 Using the same example as before where $\xi = 4$, if the amount of biomass associated
 326 with one simulated particle in the 5 m/day sinking-velocity class is taken as $B_0 = 1$, then one simulated particle sinking at 0.025 m/day contains 14.14 units of biomass
 327 and a single particle contains $14.14/40,000 = 3.5 \times 10^{-4}$ units of biomass (see Figure
 328 4). This normalized formulation of particle number and biomass (see Equations (5)
 329 and (8)) has the advantage that the impact of spectral slope on the relative export of
 330 biomass can be quantified without needing a large number of particle-tracking experi-
 331 ments, where the number of seeded particles would vary to account for the different
 332 spectral slopes. For the purpose of this study, only the relative amount of biomass is
 333 relevant. For simplicity, we define a normalized biomass unit for $\xi = 3$ as $B_0 = 1$. The
 334 values taken by B_0 for other Junge slopes ξ are computed under the condition that
 335 the total amount of biomass is kept constant (Figure 4b).
 336

337 2.2.4 Particle Remineralization Scheme

Remineralization of particles as they sink through the water column impacts the amount of biomass exported. Slow-sinking particles generally contain less biomass and spend more time in the mixed layer, which means that they are remineralized at a shallower depth than faster sinking particles. Remineralization processes are complex, species-dependent, and generally not well-understood. In the absence of a consensus on a general functional form of particle remineralization, we rely on an idealized relationship which assumes that the biomass content of a particle decreases in time proportionally to the particle volume. Remineralization is thus modeled as an exponential decrease of biomass with time at a rate k (Iversen & Ploug, 2010, 2013)

$$B(t) = B^0 \exp(-kt), \quad (9)$$

where B^0 denotes the biomass content at $t = 0$ days, and the remineralization rate is taken to be $k = 0.13 \text{ day}^{-1}$ in this study (Iversen & Ploug, 2010). This remineralization rate is independent of particle sinking velocity, and seems to lie within the range of other estimates (Iversen & Ploug, 2010, 2013; Ploug, Iversen, Koski, & Buitenhuis, 2008). The change in biomass with time is in turn expected to affect the sinking velocity of the particle. Given that $B \propto w^{3/2}$ (see Equation (6)), particles in all

sinking-velocity classes undergo a decay in sinking speed according to

$$w_s(t) = w_s^0 \exp\left(-\frac{2kt}{3}\right), \quad (10)$$

where w_s^0 is the initial sinking velocity at $t = 0$ days. In this study, the impact of remineralization is thus considered through the implementation of a time-dependent sinking velocity (Equation 10). While particles classes are classified based on their initial sinking-velocity, it is worth noting that over the length of the particle-tracking experiments that include remineralization (28 days), particle sinking speeds slow down to 10% of their initial velocity.

3 Results

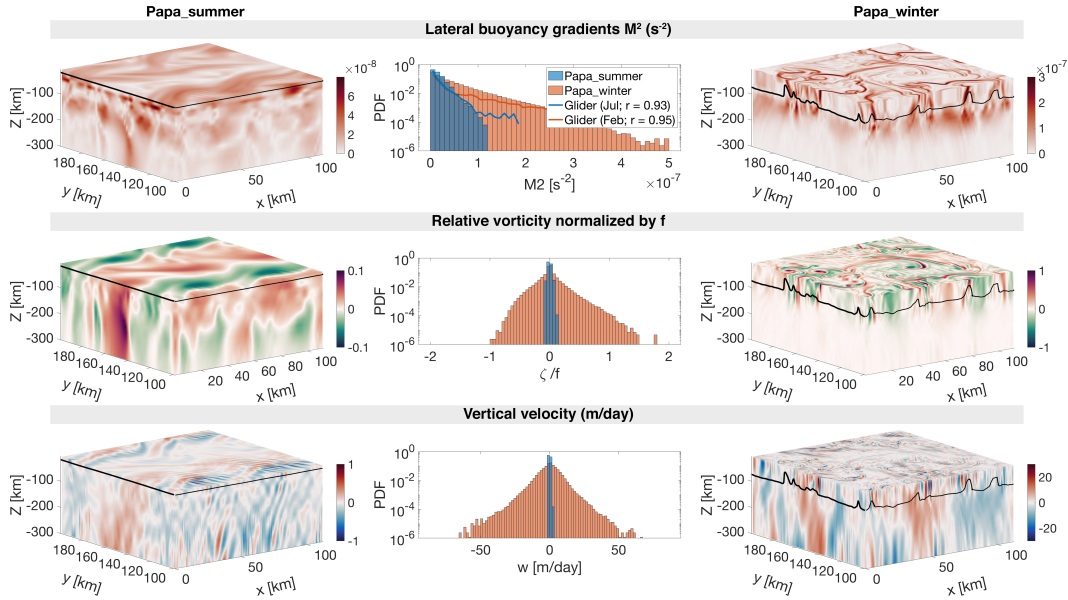
3.1 Seasonally varying dynamical regimes

Two model experiments are designed to capture different dynamical conditions observed in the Northeast Pacific Ocean in summer and winter. *Papa-summer* is initialized in early spring (doy 105) when the water column is characterized by a relatively deep mixed layer (~ 100 m) and a halocline located between 100 and 150 m (Figure 2). The forcing by a realistic, positive, net heat flux generates the restratification of the water column, with the development of a strong thermocline between 25 and 50 m leading to the shoaling of the mixed layer and a subsurface peak in N^2 at about 30 m (see Figure 2). A comparison between model outputs and monthly-averaged density profiles from underwater gliders collected in June and July over the period 2008-2009 yields correlation coefficients of $r = 0.87$ and $r = 0.88$, respectively. These high correlation suggest that *Papa-summer* numerical experiment captures the vertical spring and summer conditions in the Northeast Pacific Ocean.

In the horizontal, the prescribed density fronts progressively become unstable within the first 60 days of the experiment (Figure 2). During this time, the Total Kinetic Energy (KE_{tot}) contained in the model domain slowly increases before reaching a maximum at doy 162, where it remains relatively constant for the rest of the simulation. The flattening of the KE_{tot} curve is used to determine the time necessary for the simulation to spin-up, hence determining the start day of the particle-tracking experiments. The ocean dynamics associated with *Papa-summer* are characterized using PDFs of horizontal buoyancy gradients ($M^2 = |\nabla_H b|^2$), vertical velocities (w), and Rossby numbers computed from the normalized vertical component of the relative vorticity ($Ro = (v_x - u_y)/f$ where $f = 1.12 \times 10^{-4}$; Figure 5).

Lateral buoyancy gradients in the summer are relatively weak $\mathcal{O}(10^{-8} \text{ s}^{-2})$ and result in low Rossby numbers $\mathcal{O}(0.1)$, with positive relative vorticity on the denser (north) side of the front and negative relative vorticity on the lighter (south) side of the front. Corresponding vertical velocities are consistently weaker than 1 m/day ($< 10^{-5}$ m/s) and are characterized by regions of weak upwelling and downwelling on 10 km scales, associated with the meandering of the front (Bower & Rossby, 1989). Alternating bands of upwelling and downwelling at $\mathcal{O}(1 \text{ km})$ spatial scale are superimposed, and likely caused by propagating internal waves. Coherent vertical velocities structures extend to depths much greater than the mixed layer depth (~ 25 m; Figure 5). The amplitude of the vertical velocity field coincides with the expected order of magnitude given by the scaling $w \propto Ro f U / N$ (Mahadevan, 2016): using $Ro \sim 0.1$ (Figure 5), $N \sim 10^{-2} \text{ s}^{-1}$ (Figure 2), $f \sim 10^{-5} \text{ s}^{-1}$, and $U \sim 0.01 \text{ m/s}$, we obtain $w \sim 10^{-6} \text{ m/s}$, or $\sim 10^{-1} \text{ m/day}$.

Papa-winter is, on the other hand, initialized in the winter (doy 0) to capture a time period where the mixed layer depth is deeper (~ 100 m) and density gradients more pronounced (Pelland et al., 2016). At this time of year, the water column in this region is characterized by the presence of a deep halocline between 100 and 150



368 **Figure 5.** Snapshots of M^2 (top), ζ/f (middle), and w (bottom) half-way through the
 369 particle tracking experiment for *Papa_summer* (left) and *Papa_winter* (right), with the Mixed Layer
 370 Depth indicated by the solid black line. The corresponding Probability Distribution Functions
 371 (PDFs) are shown in the center for both *Papa_summer* (blue) and *Papa_winter* (red). Note the
 372 different colorbars used for *Papa_summer* and *Papa_winter*. Histograms of M^2 computed from
 373 glider data at Station Papa in February (blue line) and July (red line) are superimposed in the
 374 top middle panel.

392 m (Figure 3 Pelland et al., 2016). After spin-up, the vertical stratification remains
 393 consistent throughout the model run, and compares well with the vertical profile ob-
 394 tained from glider observations for the month of March ($r = 0.95$; see Figure 3). In
 395 the horizontal, prescribed density fronts are much sharper than in summer (i.e., over
 396 smaller spatial scales $O(1 \text{ km})$ vs. $O(10 \text{ km})$). Because of these stronger density
 397 gradients, combined with the alternating zonal winds and constantly negative surface
 398 heat flux, the fronts become unstable more rapidly than in summer (Figure 3). As a
 399 result, KE_{tot} starts to plateau at doy 48. The experiment is considered spun-up by
 400 doy 50 and the particle-tracking experiment is initialized.

401 The frontal structures visible in the horizontal buoyancy gradient field are as-
 402 sociated with filaments of relatively high Rossby number of $\mathcal{O}(1)$ (Figure 5). The
 403 PDF of relative vorticity reveals a positively-skewed distribution ($s = 0.68$). This is in
 404 agreement with the fact that the relative vorticity is more likely to be cyclonic than an-
 405 ticyclonic, based on conservation of potential vorticity (Hoskins & Bretherton, 1972).
 406 Regions with high Rossby number are localized and located in the mixed layer exclu-
 407 sively. In places where the local Rossby number reaches $\mathcal{O}(1)$, geostrophic balance is
 408 lost and a vertical secondary ageostrophic circulation begins to slump the isopycnals
 409 and restore the flow to a more geostrophically-balanced flow. This ageostrophic sec-
 410 ondary circulation therefore generates “hot spots” of higher vertical velocities. The
 411 fine-scale structures in the vertical velocity field corresponding to $\mathcal{O}(1)$ Rossby num-
 412 bers can be seen in Figure 5, with local vertical velocities up to 60 m/day ($\sim 7 \times 10^{-4}$
 413 m/s). Contrary to the PDF of relative vorticity, the distribution of vertical velocities
 414 demonstrate a negative skewness ($s = -0.25$). This is in agreement with the theory:
 415 In fact, positive relative vorticity is associated with the dense side of a density front,

416 where vertical velocities are negative (Mahadevan, 2016). Once again, the amplitude
 417 of these vertical velocity hot spots is coherent with the scaling $w \propto Ro f U / N$: using
 418 $Ro \sim 1$, $N \sim 10^{-2}$ 1/s, $f \sim 10^{-5}$ 1/s, and $U \sim 0.1$ m/s, we obtain $w \sim 10^{-4}$ m/s, or
 419 $\sim 10^1$ m/day.

420 Comparing *Papa-summer* and *Papa-winter* highlights the different dynamical
 421 regimes in the two experiments. In *Papa-winter*, density fronts tend to be sharper,
 422 meaning larger density gradients over shorter spatial scales. When computed at the
 423 kilometer-scale, the PDF of horizontal buoyancy gradients in *Papa-winter* exhibits a
 424 longer tail than in *Papa-summer* (Figure 5). When compared to observations, the
 425 PDFs of M^2 in *Papa-summer* and *Papa-winter* demonstrate a correlation with obser-
 426 vations of $r = 0.93$ and $r = 0.95$, respectively.

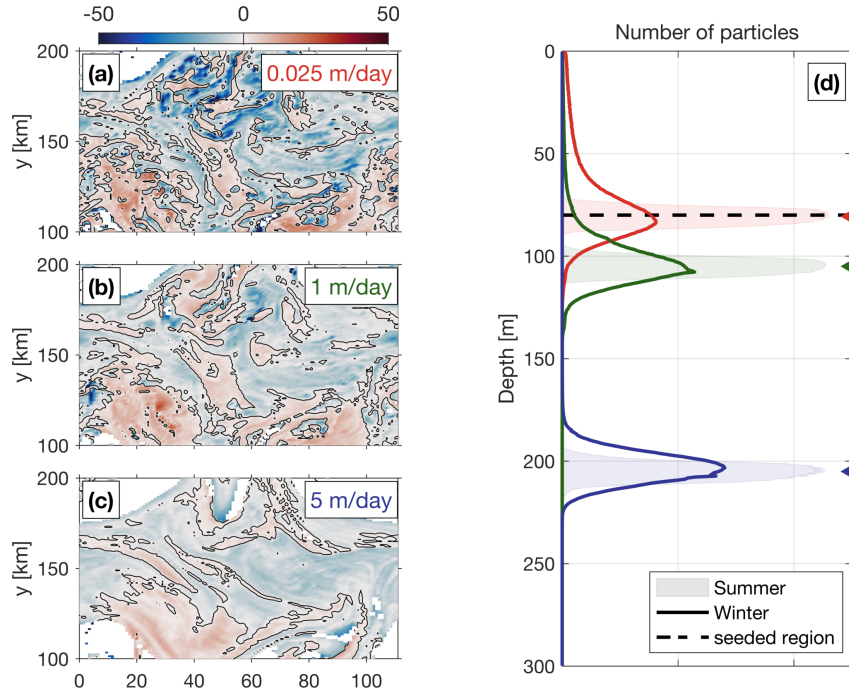
427 The wider PDF of vertical velocities in *Papa-winter* shows advective velocities
 428 that match and exceed typical gravitational sinking velocities, particularly for smaller,
 429 and therefore slower-sinking, particulate organic material. The secondary ageostrophic
 430 circulation that develops at submeso-scales (i.e., $Ro \mathcal{O}(1)$) therefore generates an ex-
 431 port mechanism that directly competes with the traditional paradigm that relies on
 432 gravitational sinking leading the export of particulate matter in the ocean.

433 3.2 Gravitational and Advective Export of POC

434 Both model experiments described above were then used to investigate the re-
 435 lationship between ocean dynamics and particle downward flux, using Lagrangian
 436 particle-tracking. Domain-averaged, downward particle flux is expected to be a com-
 437 bination of the flux driving by gravitational sinking ($\langle w_s B \rangle$), and by the vertical ad-
 438 vective currents affecting the particle along its pathway ($\langle wB \rangle$). The deviation in
 439 particle depths from the traditional one-dimensional gravitationally driven model is
 440 shown in Figure 6 for both summer and winter cases. In the summer, the PDF of par-
 441 ticle density versus depth remains relatively narrow through time, and is centered on
 442 a depth level that can be predicted using a simple 1D gravitational model (see shaded
 443 curves in Figure 6). The spread in the particle density also vary little among particle
 444 classes with different sinking velocities, suggesting that downward fluxes of particles
 445 is greatly dominated by gravitational settling and is not subject to significant vertical
 446 ocean currents.

457 In the winter, however, PDFs of particle density versus depth is wider, in agree-
 458 ment with the stronger vertical ocean currents occurring in the winter (see Figure 5).
 459 A top-view of the deviation in the downward particle flux from the traditionally con-
 460 sidered 1D gravitational model can be seen in Figure 6 (panels (a)-(c)). Slower-sinking
 461 particles deviate more than faster-sinking particles, exhibiting median depth anom-
 462 alies up to 50 m. This is due to the fact that slower-sinking particles spend more time
 463 in the mixed layer, where most of the stronger vertical currents tend to occur (Figure
 464 5). An interesting result emerges from the spatial distribution of the depth-anomaly:
 465 both positive (i.e., particles are shallower than expected) and negative (i.e., particles
 466 are deeper than expected) anomalies are organized into features with a length-scale
 467 $\mathcal{O}(1\text{-}10 \text{ km})$. This further highlights the importance of winter submesoscale circulation
 468 for vertical fluxes of particles.

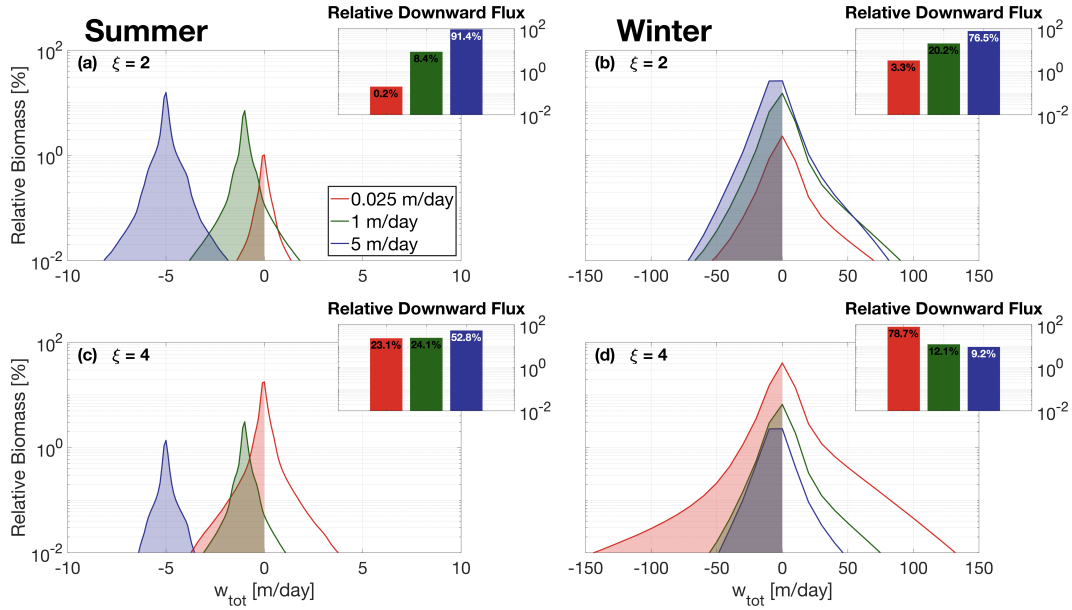
469 A relative amount of biomass is associated to the particles using Equation (8).
 470 PDFs of relative biomass as a function of the vertical velocity is shown in Figure 7.
 471 Following the traditional paradigm derived from the simple 1D gravitational model, the
 472 downward flux of biomass in the summer is dominated by faster-sinking particle classes
 473 capable of carrying particulate material downwards more efficiently. The contribution
 474 of slower-sinking particles, however, depends critically on the slope of the size spectrum
 475 (see Figure 4). As the Junge slope increases, the spectrum of biomass steepens, and
 476 the relative contribution of slower-sinking particles to the downward biomass flux



447 **Figure 6.** [left] The median depth anomaly of particles with a sinking speed (a) 0.025 m/d,
448 (b) 1 m/d, (c) 5 m/d within each grid cell for the winter case 25 days after particles are released.
449 The ‘depth anomaly’ is with respect to the ‘expected’ sinking depth (= sinking speed \times time
450 since release). Blue (red) grid cells indicate that the median depth of particles in this cell is
451 deeper (shallower) than expected, based on a 1D gravitational model where $z = w_s \times t$. [right]
452 (d) Probability Distribution Function (PDF) of particles as a function of depth for each velocity
453 class. The winter distribution is shown as thick lines, while the summer distribution is repre-
454 sented by the shaded regions. Triangle markers indicate the expected depth of particles after 25
455 days based on the 1D gravitational model, which is used as a reference to compute the depth
456 anomalies. Release depth is indicated by the thick dashed line.

477 significantly increases (Figure 7c). In fact, the contribution of slower-sinking particles
478 to the summer downward flux increases by a factor 100 (from 0.1% to 10%) when the
479 Junge slope varies from $\xi = 2$ to $\xi = 4$. While significant, the impact of a change in
480 the Junge slope in summer conditions does not challenge the dominant role played by
481 faster-sinking particles. This result can be explained by the fact that, in the summer,
482 vertical velocities are weak and vertical biomass fluxes are therefore gravitationally-
483 driven ($\langle w_s B \rangle > \langle w B \rangle$).

491 In the winter, PDFs of relative biomass as a function of vertical velocities present
492 a much larger spread, with velocity magnitudes exceeding 50 m/day. For $\xi = 2$,
493 the relative contribution of slower-sinking particles to the downward flux significantly
494 increases from 0.1% in the summer to about 4% in the winter, demonstrating the
495 impact advective velocities alone can have on vertical fluxes (Figure 7b). Nevertheless,
496 slower-sinking particles remain a relatively small contributor to the total downward
497 flux of biomass. When winter ocean dynamics are coupled with a steeper Junge slope,
498 however, slower-sinking particles largely dominate the downward biomass flux. In
499 our winter simulations with $\xi = 4$, we find that the slowest-sinking particle class is
500 responsible for about 80% of the biomass flux (Figure 7d).

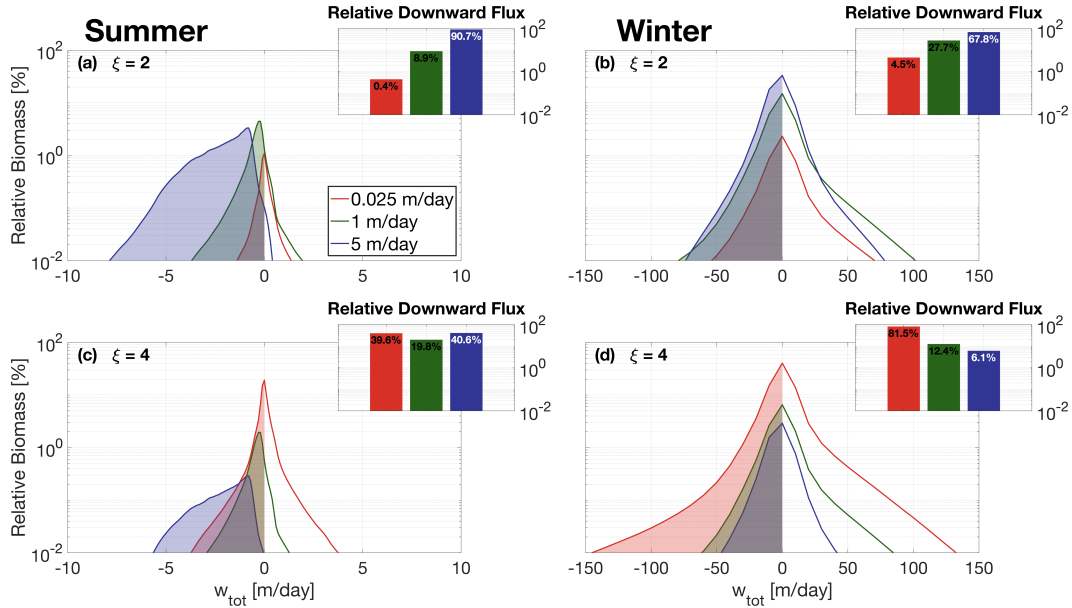


484 **Figure 7.** Probability Distribution Function (PDF) of relative biomass versus total vertical
 485 velocity ^{c3}(sinking + advective) along particle trajectories in the summer case [left] and winter
 486 case [right], with a Junge slope of 2 [top] and 4 [bottom]. ^{c4}PDFs are computed from the whole
 487 24-day particle tracking experiments. Inserts show the integrated relative downward biomass flux
 488 associated with each sinking-velocity class, categorized according to their initial sinking veloc-
 489 ity. Both winter dynamics and steeper Junge slopes tend to increase the relative contribution of
 490 slower-sinking particles.

501 Our results show that both a steepening of the particle size spectrum and the
 502 presence of submesoscale dynamics can enhance the contribution of slower-sinking par-
 503 ticles to the downward biomass flux. While the former is simply due to an increase in
 504 particle density in slower-sinking particle classes, the latter is attributed to the larger
 505 vertical velocity generated by submesoscale instabilities. When both are combined,
 506 as expected in the wintertime, slower-sinking particles then become the leading con-
 507 tributor to the downward biomass transport. However, slower-sinking particles are
 508 generally expected to remineralize on timescales shorter than their export timescale,
 509 fueling the argument that the focus should be upon faster-sinking particle classes. The
 510 impacts of remineralization on export are thus considered in the following section to
 511 test the robustness of the findings.

512 3.3 Particle Remineralization

513 Both submesoscale dynamics and the Junge slope were identified as key factors
 514 impacting the respective role played by different particle classes in driving downward
 515 biomass fluxes. Simple Lagrangian particles were used to isolate the effects of these
 516 two factors. In reality, however, sinking velocities of particulate matter varies in time
 517 as the particles slowly remineralize. A remineralizing behavior was therefore imple-
 518 mented for the Lagrangian particles, using Equation (10), to investigate the impact
 519 that remineralization processes have on our findings. The traditional paradigm relies
 520 on the fact that slow-sinking particles tend to fully remineralize over short timescales,
 521 further enhancing the importance of faster-sinking particles classes in driving down-
 522 ward biomass fluxes. While this paradigm holds for flatter Junge slope, where the



539 **Figure 8.** Same as Figure 7, but including particle remineralization (see Equation 10).

523 biomass content is dominated by faster-sinking particles, it becomes unfit at steeper
524 slopes.

525 Figure 8 compares the relative biomass and downward biomass fluxes associated
526 with each of the modeled particle classes for $\xi = 4$ with and without the remineraliza-
527 tion scheme. As previously detailed, downward fluxes of biomass are dominated
528 by faster-sinking particles during summertime and in the absence of remineralization.
529 This is due to the fact that the flux of biomass $\langle w_{tot}B \rangle = \langle w_s B \rangle + \langle w B \rangle$ is driven by
530 $\langle w_s B \rangle$, despite a smaller relative biomass content per particle. This is characteristic
531 of a gravitationally-driven system, where settling velocity dictates the contribution to
532 downward fluxes. Implementing remineralization processes, however, directly affects
533 the particle settling velocity which slows down as particles remineralize. This effect
534 can be seen in Figure 8c, where PDFs of relative biomass per particle class are shifted
535 towards weaker vertical velocities than in the absence of remineralization, as predicted
536 by Equation (10). As a result, the gravitationally-driven term $\langle w_s B \rangle$ decreases with
537 time, and the downward flux of biomass becomes generally advectively-driven by day
538 25 (Figure 8).

540 In an advectively-driven system where $\langle w_s B \rangle < \langle w B \rangle$, the relative amount of
541 biomass content in a particle class becomes important and dictates the respective con-
542 tribution of each particle class to the total downward biomass fluxes. This shift from a
543 gravitationally-driven to an advectively-driven system is observed when implement-
544 ing particle remineralization in the summer (Figure 8c): in the absence of remineralization,
545 faster-sinking particles dominate the downward biomass fluxes (60%; see Figure 8a).
546 When remineralization processes are considered, slower-sinking particles become the
547 dominant contributor to biomass fluxes (see inset in Figure 8c). As shown in Figure
548 7, downward biomass fluxes in the wintertime are generally advectively-driven, due
549 to the larger vertical velocities associated with wintertime ocean dynamics. Biomass
550 fluxes are dominated by the slower-sinking particles, representing 82% of the down-
551 ward biomass flux (Figure 8b). Even after implementing our remineralization scheme,
552 slower-sinking particles remain the largest contributor to downward biomass fluxes
553 (87%; see Figure 8d).

These results highlight the importance in considering slower-sinking particle classes when considering downward biomass fluxes. It also demonstrates that, contrarily to the traditional paradigm, remineralization processes enhance the role played by slower-sinking particles in biomass fluxes, in cases where the biomass spectrum slope is negative.

The timescales over which the system transitioned from an gravitationally-driven to an advectively-driven system depends on the remineralization model used.

4 Discussion

4.1 Dynamical Regimes

Papa-summer and *Papa-winter* experiments were designed to statistically capture the ocean dynamics at Station Papa (145°W, 50°N) in the Northeast Pacific Ocean. After spin-up, the model demonstrated similar distributions of both horizontal (M^2) and vertical (N^2) density gradients to observational estimates from underwater gliders (see Figures 2, 3, and 5). The two experiments, however, show significantly different distributions of M^2 , with the winter distribution exhibiting a longer tail, due to sharper density gradients. The tail of the wintertime distribution is only partially captured by the glider data, due to the fact that underwater gliders sampled gradients at spatial scales of 10 km and greater, while the model has a horizontal resolution of 500 m, allowing sharper submesoscale fronts and filaments to be formed.

Studies investigating submesoscale dynamics traditionally focused on regions where the presence of submesoscale fronts and filaments are established, such as western boundary currents with strong gradients (D'Asaro, Lee, Rainville, Harcourt, & Thomas, 2011; Thomas, Tandon, & Mahadevan, 2013), or the edge of mesoscale features (van Haren et al., 2006; Waite et al., 2016). The seasonality in submesoscale dynamics captured in the glider dataset at Station Papa and reflected in the model experiments, echoes the behavior seen from recent observational studies conducted at a similar latitude in the Atlantic Ocean, which demonstrate the intensification of submesoscale dynamics in the wintertime (Buckingham et al., 2016; Thompson et al., 2016). Despite being sometimes qualified as an “eddy desert” with low kinetic energy (Chelton, Schlax, & Samelson, 2011), ocean characteristics in the eastern part of the Pacific subpolar gyre suggest the presence of submesoscale features in the wintertime: strong density gradients, localized Rossby numbers of order 1, a balanced Richardson number $Ri_b = \frac{f^2 N^2}{M^4}$ smaller than 1, a positively skewed distribution in vorticity, and a negatively skewed distribution of vertical velocities (see Figure 5; Buckingham et al., 2016; Rudnick, 2001; Thomas, Taylor, et al., 2013).

Strong downward velocities are hypothesized to enhance POC export by advecting slower-sinking particles out of the mixed layer. *Papa-winter* indeed exhibits vertical velocities more than 20 times larger than in *Papa-summer*. The vertical currents in *Papa-winter*, however, tend to be much patchier than the weaker vertical currents observed in *Papa-summer*. Because both particle production and downward vertical velocities present a high degree of patchiness, it requires a certain level of covariance between the two fields for the export to effectively be enhanced (Mahadevan et al., 2012). A more realistic seeding strategy for Lagrangian particles, such as one guided by biological tracers, would likely provide important information towards a better understanding of the effects of patchiness on POC export at submeso-scales

The hypothesis tested in this study is that submesoscale activity enhances export of particulate matter at Station Papa by shortening the export timescale of particulate matter. The wintertime intensification in submesoscale activity has the potential to indeed enhance export (see discussion in Section 4.2). However, the seasonal cycle in submesoscale activity is out of phase with the one in net community productivity,

which peaks in the spring and summertime when the mixed layer is shallower (Plant et al., 2016). Two mechanisms are therefore present to potentially sustain a year-long POC export flux: In the winter, less particulate material is present in the mixed layer, but active submesoscale dynamics tend to enhance the POC export flux by advecting the more numerous slower-sinking particles into the ocean interior. In the summer, the production of POC is at its yearly maximum, but export tends to be dominated by gravitational sinking, which favors faster-sinking particles and thus exclude part of the particle spectrum from contributing to the export flux.

612 4.2 Downward Fluxes

Analyses of particle tracking experiments reveal that the contribution of slower-sinking particles to the downward particulate flux depends on two main factors: (1) the dynamics of the oceanic flow field, and (2) the slope of the size spectrum (i.e., the Junge slope ξ).

Mixed layer ocean dynamics at station Papa change significantly between the winter and the summer. In the winter, submesoscale dynamics are intensified, and sharp fronts and filaments develop in the mixed layer. This seasonal change in dynamics is consistent with recent observations (Buckingham et al., 2016; Thompson et al., 2016), and models (Brannigan, Marshall, Naveira-Garabato, & George Nurser, 2015; Callies et al., 2015; Rocha, Gille, Chereskin, & Menemenlis, 2016) characterizing the seasonal cycle of submesoscale dynamics. The winter intensification in submesoscale dynamics was proven to have an important impact on the downward flux of all sinking-velocity classes modeled in this experiment.

In the summer, gravitational sinking governs a downward particulate flux, which is dominated by faster-sinking particles, with little to no contribution from slower-sinking particles. In the winter, however, vertical fluxes tend to be advectively-driven, which leads to a slightly weaker downward flux of faster-sinking particles than in the summer due to resuspension, but a much larger flux of slower-sinking particles, which are present in far greater numbers (Figure 7). The gravitationally-driven flux in the summer is mechanistically different from the advectively-driven winter flux, which raises the question as to which process is most efficient in driving a downward flux of particulate material.

In the absence of remineralization, both a steeper size spectrum slope ($\xi > 3$ in this case) and enhanced submesoscale dynamics, increase the contribution of slower-sinking particle classes to the downward biomass flux. This is only when both of these conditions are combined, however, that slower-sinking particles dominate the downward flux of biomass (Figure 7). This is a significant result, as Junge slopes greater than 3 have been observed in the ocean ^{c1}: In-situ observations yield average spectral slopes varying between 3.5 and 4.5 (Kostadinov, Siegel, & Maritorena, 2009, see Table 2 in ^{c2}, while spectral analysis of satellite data suggest global spectral slopes varying between 3 and 6. More recent observational work located in the Northeast Pacific, including Station Papa, found a spectral slope also greater than 3(White et al., 2015, ; Z. Xiaodong, personal communication). ^{c3}Junge slopes are expected to vary in space, depending on the community composition, both lateraly and vertically (Kostadinov et al., 2009; White et al., 2015)^{c4}, as well as in time; spectrum slopes tend to be flatter during a spring bloom event, where larger particles (e.g., diatoms) are produced in large quantities (cite cite cite), and steeper during the wintertime, when communities

^{c1} *Text added.*

^{c2} *Text added.*

^{c3} *Text added.*

^{c4} *Text added.*

650 are mostly composed of small particles (cite cite cite). The threshold value of $\xi = 3$ for
 651 a change in the biomass spectral slope (see Figure 4b) is of course a consequence of first-
 652 order approximations used in this study describing the relationships between particle
 653 size, sinking velocity, and biomass content. Nevertheless, our results demonstrate the
 654 importance of including the smaller particle size range of the particle spectrum, in the
 655 estimation or measurement of vertical fluxes, especially when submesoscale dynamics
 656 are active. It also highlights the importance of better constraining the relationships
 657 linking particle size, sinking velocity, and biomass content.

658 Introducing remineralization processes significantly decreases the biomass flux.
 659 Counter-intuitively, however, the implementation of a remineralization scheme further
 660 strengthens the contribution of slower-sinking particles to the biomass flux (Figure
 661 8). This can be explained by the fact that remineralization processes have a greater
 662 impact on sinking-velocity classes that rely on gravitational sinking to be exported, as
 663 these particles decelerate as they remineralize. In the summer, all particle classes are
 664 similarly affected by remineralization, as downward fluxes are gravitationally-driven.
 665 In the winter, however, slower-sinking particles are exported through advective pro-
 666 cesses. Their export timescale is barely affected by remineralization processes as it
 667 only depends on local ocean dynamics.

668 The results of this study suggest that slow- and non-sinking particles must be
 669 considered when studying the downward flux of particulate matter in the upper ocean.
 670 The patchiness associated with both particle production and submesoscale features
 671 poses a real observational challenge to properly resolve vertical fluxes. Based on our
 672 findings, subsequent studies should focus on testing the impact of patchiness on vertical
 673 fluxes. In the wintertime, when size spectral slope is steep and submesoscale dynamics
 674 most active, vertical fluxes could be grossly underestimated depending on the level of
 675 co-occurrence between particle production and stronger vertical currents.

676 5 Conclusion

677 The main conclusions of this study are:

- 678 1. Ocean dynamics in the subpolar Northeast Pacific exhibit a seasonal cycle with
 679 low submesoscale activity in the summertime, and more submesoscale features
 680 present in the wintertime. Submesoscale dynamics generate larger, and asym-
 681 metric, vertical currents leading to a vertical biomass flux driven by advective
 682 processes, as opposed to gravitational sinking in the summertime.
- 683 2. Submesoscale dynamics generally enhance the downward particulate flux by
 684 increasing the contribution of slower-sinking particles to the total flux through
 685 advective transport. The slower-sinking particles are found to be significant
 686 for export, and can be even make the dominant contribution under certain
 687 conditions.
- 688 3. The contribution of slower-sinking particles to the downward biomass flux de-
 689 pends on the slope of the particle size spectra (i.e., the Junge Slope), that
 690 controls the relative number of particles per size class. Two cases emerge from
 691 this study:
 - 692 (a) If the Junge slope is smaller than 3, larger particles contribute most to vertical
 693 biomass fluxes independently of flow dynamics, as there are no mechanisms
 694 capable of selectively advecting slower-sinking particles. The system is de-
 695 scribed as gravitationally-driven.
 - 696 (b) If the Junge slope is greater than 3, as most commonly observed, ocean
 697 dynamics become key for determining which particle classes dominate the
 698 downward flux. As submesoscale dynamics become more active, ageostrophic
 699 circulations leading to larger vertical velocities develop. In these conditions,

700 downward biomass fluxes are largely driven by the slower-sinking particle
 701 classes.

702 4. Remineralization processes logically reduce the amount of biomass flux. How-
 703 ever, it unexpectedly enhances the role of slower-sinking particles, which are are
 704 advectively transported. The impact of remineralization is greater on faster-
 705 sinking particles since it affects both the biomass content and their sinking
 706 velocity.

707 Acknowledgments

708 The work was funded by NASA grant NNX16AR48G, to complement the EXport
 709 Processes in the global Ocean from RemoTe Sensing (EXPORTS) program. We would
 710 like to thank A. Thompson (Caltech) for his useful comments and suggestions, N.
 711 Pelland (NOAA) and C. Eriksen (University of Washington) for sharing the glider data
 712 collected at Ocean Station Papa, as well as S. Essink for his assistance in developing the
 713 particle-tracking code. All data used in this manuscript are publicly available: Ocean
 714 Station Papa data is available on PMEL's website (<https://www.pmel.noaa.gov/ocs/Papa>; PMEL, 2018) and gridded Argo products can be downloaded at <http://www.seanoe.org/data/00348/45945> (Gaillard, 2015). Glider data is archived at the
 715 University of Washington's Library (<http://hdl.handle.net/1773/41656>; Pelland,
 716 2018).

719 References

- 720 Alkire, M., D'Asaro, E., Lee, C., Perry, M., Gray, A., Cetinic, I., ... González-
 721 Posada, A. (2012). Estimates of net community production and export using
 722 high-resolution, Lagrangian measurements of O₂, NO₃⁻, and POC through the
 723 evolution of a spring diatom bloom in the North Atlantic. *Deep-Sea Res. I*,
 724 64, 157-174. doi: 10.1016/j.dsr.2012.01.012
- 725 Bach, L. T., Riebesell, U., Sett, S., Febiri, S., Rzepka, P., & Schulz, K. G. (2012).
 726 An approach for particle sinking velocity measurements in the 3400 μm size
 727 range and considerations on the effect of temperature on sinking rates. *Marine
 728 Biology*, 159(8), 1853–1864. doi: 10.1007/s00227-012-1945-2
- 729 Bower, A. S., & Rossby, T. (1989). Evidence of Cross-Frontal Exchange Processes
 730 in the Gulf Stream Based on Isopycnal RAFOS Float Data. *Journal of Phys-
 731 ical Oceanography*, 19(9), 1177–1190. doi: 10.1175/1520-0485(1989)019<1177:
 732 EOCFEP>2.0.CO;2
- 733 Brannigan, L., Marshall, D. P., Naveira-Garabato, A., & George Nurser, A. (2015).
 734 The seasonal cycle of submesoscale flows. *Ocean Modelling*, 92, 69–84. doi: 10
 735 .1016/j.ocemod.2015.05.002
- 736 Briggs, N., Perry, M. J., Cetini, I., Lee, C., D'Asaro, E., Gray, A. M., & Rehm, E.
 737 (2011). High-resolution observations of aggregate flux during a sub-polar north
 738 atlantic spring bloom. *Deep Sea Research Part I: Oceanographic Research
 739 Papers*, 58(10), 1031 - 1039. doi: 10.1016/j.dsr.2011.07.007
- 740 Buckingham, C. E., Naveira Garabato, A. C., Thompson, A. F., Brannigan, L.,
 741 Lazar, A., Marshall, D. P., ... Belcher, S. E. (2016). Seasonality of sub-
 742 mesoscale flows in the ocean surface boundary layer. *Geophysical Research
 743 Letters*, 43(5), 2118–2126. doi: 10.1002/2016GL068009
- 744 Callies, J., Ferrari, R., Klymak, J. M., & Gula, J. (2015). Seasonality in sub-
 745 mesoscale turbulence. *Nature communications*, 6, 6862. doi: 10.1038/
 746 ncomms7862
- 747 Chelton, D. B., Schlax, M. G., & Samelson, R. M. (2011). Global observations of
 748 nonlinear mesoscale eddies. *Progress in Oceanography*, 91(2), 167–216. doi: 10
 749 .1016/j.pocean.2011.01.002

- D'Asaro, E., Lee, C., Rainville, L., Harcourt, R., & Thomas, L. (2011). Enhanced turbulence and energy dissipation at ocean fronts. *Science*, 332(6027), 318–322. doi: 10.1126/science.1201515
- Döös, K., Kjellsson, J., & Jönsson, B. (2013). TRACMASS – A Lagrangian Trajectory Model. In *Preventive methods for coastal protection* (pp. 225–249). Heidelberg: Springer International Publishing. doi: 10.1007/978-3-319-00440-2_7
- Ducklow, H. W., Steinberg, D. K., & Buesseler, K. O. (2001). Upper Ocean Carbon Export and the Biological Pump. *Oceanography*, 14. doi: <https://doi.org/10.5670/oceanog.2001.06>
- Estapa, M. L., Siegel, D. A., Buesseler, K. O., Stanley, R. H. R., Lomas, M. W., & Nelson, N. B. (2015). Decoupling of net community and export production on submesoscales in the Sargasso Sea. *Global Biogeochemical Cycles*, 29(8), 1266–1282. doi: 10.1002/2014GB004913
- Falkowski, P. G., Barber, R. T., & Smetacek, V. (1998). Biogeochemical Controls and Feedbacks on Ocean Primary Production. *Science*, 281(5374), 200–206. doi: 10.1126/science.281.5374.200
- Fox-Kemper, B., Ferrari, R., & Hallberg, R. (2008). Parameterization of Mixed Layer Eddies. Part I: Theory and Diagnosis. *Journal of Physical Oceanography*, 38(6), 1145–1165. doi: 10.1175/2007JPO3792.1
- Gaillard, F. (2015). ISAS-13 temperature and salinity gridded fields. SEANOE. doi: 10.17882/45945
- Gaillard, F., Reynaud, T., Thierry, V., Kolodziejczyk, N., & von Schuckmann, K. (2016). In situ-based reanalysis of the global ocean temperature and salinity with isas: Variability of the heat content and steric height. *Journal of Climate*, 29(4), 1305–1323. doi: 10.1175/JCLI-D-15-0028.1
- Gruber, N., Lachkar, Z., Frenzel, H., Marchesiello, P., Münnich, M., McWilliams, J. C., ... Plattner, G.-K. (2011). Eddy-induced reduction of biological production in eastern boundary upwelling systems. *Nature geoscience*, 4(11), 787. doi: 10.1038/NGEO1273
- Harrison, P. J., Whitney, F. A., Tsuda, A., Saito, H., & Tadokoro, K. (2004). Nutrient and Plankton Dynamics in the NE and NW Gyres of the Subarctic Pacific Ocean. *Journal of Oceanography*, 60(1), 93–117. doi: 10.1023/B:JOCE.0000038321.57391.2a
- Hoskins, B. J., & Bretherton, F. P. (1972). Atmospheric Frontogenesis Models: Mathematical Formulation and Solution. *Journal of the Atmospheric Sciences*, 29(1), 11–37. doi: 10.1175/1520-0469(1972)029<0011:AFMMFA>2.0.CO;2
- Iversen, M. H., & Ploug, H. (2010). Ballast minerals and the sinking carbon flux in the ocean: carbon-specific respiration rates and sinking velocity of marine snow aggregates. *Biogeosciences*, 7(9), 2613–2624. doi: 10.5194/bg-7-2613-2010
- Iversen, M. H., & Ploug, H. (2013). Temperature effects on carbon-specific respiration rate and sinking velocity of diatom aggregates - potential implications for deep ocean export processes. *Biogeosciences*, 10(6), 4073–4085. doi: 10.5194/bg-10-4073-2013
- Klein, P., & Lapeyre, G. (2009). The Oceanic Vertical Pump Induced by Mesoscale and Submesoscale Turbulence. *Annual Review of Marine Science*, 1(1), 351–375. doi: 10.1146/annurev.marine.010908.163704
- Kostadinov, T. S., Siegel, D. A., & Maritorena, S. (2009). Retrieval of the particle size distribution from satellite ocean color observations. *Journal of Geophysical Research*, 114(C9), C09015. doi: 10.1029/2009JC005303
- Lévy, M., Ferrari, R., Franks, P. J. S., Martin, A. P., & Rivière, P. (2012). Bringing physics to life at the submesoscale. *Geophysical Research Letters*, 39(14), n/a–n/a. doi: 10.1029/2012GL052756
- Lévy, M., Klein, P., & Treguier, A.-M. (2001). Impact of sub-mesoscale physics on production and subduction of phytoplankton in an oligotrophic regime. *Journal of marine research*, 59(4), 535–565. doi: 10.1357/002224001762842181

- 805 Mahadevan, A. (2016). The Impact of Submesoscale Physics on Primary Productivity of Plankton. *Annual Review of Marine Science*, 8(1), 161–184. doi: 10.1146/annurev-marine-010814-015912
- 806
807
808 Mahadevan, A., & Archer, D. (2000). Modeling the impact of fronts and mesoscale circulation on the nutrient supply and biogeochemistry of the upper ocean. *Journal of Geophysical Research: Oceans*, 105(C1), 1209-1225. doi: 10.1029/1999JC900216
- 812 Mahadevan, A., D'Asaro, E., Lee, C., & Perry, M. J. (2012). Eddy-Driven Stratification Initiates North Atlantic Spring Phytoplankton Blooms. *Science*, 337(6090), 54–58. doi: 10.1126/science.1218740
- 813
814
815 Mahadevan, A., Oliger, J., & Street, R. (1996a). A Nonhydrostatic Mesoscale Ocean Model. Part II: Numerical Implementation. *Journal of Physical Oceanography*, 26(9), 1881–1900. doi: 10.1175/1520-0485(1996)026<1881:ANMOMP>2.0.CO; 2
- 816
817
818 Mahadevan, A., Oliger, J., & Street, R. (1996b). A Nonhydrostatic mesoscale ocean model. Part I: Well-posedness and scaling. *Journal of Physical Oceanography*, 26(9), 1868–1880. doi: 10.1175/1520-0485(1996)026<1868:ANMOMP>2.0.CO; 2
- 819
820
821 Mahadevan, A., & Tandon, A. (2006). An analysis of mechanisms for submesoscale vertical motion at ocean fronts. *Ocean Modelling*, 14(3-4), 241–256. doi: 10.1016/J.OCEMOD.2006.05.006
- 822
823
824 McDonnell, A. M. P., & Buesseler, K. O. (2010). Variability in the average sinking velocity of marine particles. *Limnology and Oceanography*, 55(5), 2085–2096. doi: 10.4319/lo.2010.55.5.2085
- 825
826 McWilliams, J. C. (2016). Submesoscale currents in the ocean. *Proceedings of the Royal Society A: Mathematical, Physical and Engineering Science*, 472(2189). doi: 10.1098/rspa.2016.0117
- 827
828 Mensa, J. A., Garraffo, Z., Griffa, A., Özgökmen, T. M., Haza, A., & Veneziani, M. (2013). Seasonality of the submesoscale dynamics in the Gulf Stream region. *Ocean Dynamics*, 63(8), 923–941. doi: 10.1007/s10236-013-0633-1
- 829
830 Mesinger, F., DiMego, G., Kalnay, E., Mitchell, K., Shafran, P. C., Ebisuzaki, W., ... Shi, W. (2006). North american regional reanalysis. *Bulletin of the American Meteorological Society*, 87(3), 343-360. doi: 10.1175/BAMS-87-3-343
- 831
832 Omand, M. M., D'Asaro, E. A., Lee, C. M., Perry, M. J., Briggs, N., Cetini, I., & Mahadevan, A. (2015). Eddy-driven subduction exports particulate organic carbon from the spring bloom. *Science*, 348(6231), 222–225. doi: 10.1126/science.1260062
- 833
834 Pelland, N. (2018). *Seaglider Surveys at Ocean Station Papa: Bin-Averaged Profiles, Currents, and Independent Oxygen Data*. Retrieved from <http://hdl.handle.net/1773/41656>
- 835
836
837 Pelland, N., Eriksen, C., & Cronin, M. (2016). Seaglider surveys at Ocean Station Papa: Circulation and watermass properties in a meander of the North Pacific Current. *Journal of Geophysical Research: Oceans*, 121, 6816–6846. doi: 10.1002/2016JC011920
- 838
839 Plant, J. N., Johnson, K. S., Sakamoto, C. M., Jannasch, H. W., Coletti, L. J., Riser, S. C., & Swift, D. D. (2016). Net community production at Ocean Station Papa observed with nitrate and oxygen sensors on profiling floats. *Global Biogeochemical Cycles*, 30(6), 859–879. doi: 10.1002/2015GB005349
- 840
841 Ploug, H., Iversen, M. H., Koski, M., & Buitenhuis, E. T. (2008). Production, oxygen respiration rates, and sinking velocity of copepod fecal pellets: Direct measurements of ballasting by opal and calcite. *Limnology and Oceanography*, 53(2), 469–476. doi: 10.4319/lo.2008.53.2.0469
- 842
843 PMEL. (2018). *Pacific Marine Environment Laboratory Ocean Climate Stations Mooring Data*. Retrieved from <https://www.pmel.noaa.gov/ocs/data-overview>

- 860 Rocha, C. B., Gille, S. T., Chereskin, T. K., & Menemenlis, D. (2016). Seasonal-
861 ity of submesoscale dynamics in the Kuroshio Extension. *Geophysical Research
862 Letters*, *43*(21), 11,304–11,311. doi: 10.1002/2016GL071349
- 863 Rudnick, D. L. (2001). On the skewness of vorticity in the upper ocean. *Geophysical
864 Research Letters*, *28*(10), 2045–2048. doi: 10.1029/2000GL012265
- 865 Sheldon, R., Prakash, A., & Sutcliffe, W., Jr. (1972). The size distribution or parti-
866 cles in the ocean. *Limnology and Oceanography*, *17*(3), 327–340. doi: 10.4319/
867 lo.1972.17.3.0327
- 868 Sherry, N. D., Boyd, P. W., Sugimoto, K., & Harrison, P. J. (1999). Seasonal and
869 spatial patterns of heterotrophic bacterial production, respiration, and biomass
870 in the subarctic NE Pacific. *Deep-Sea Research Part II: Topical Studies in
871 Oceanography*, *46*(11–12), 2557–2578. doi: 10.1016/S0967-0645(99)00076-4
- 872 Thomas, L. N., Tandon, A., & Mahadevan, A. (2013). Submesoscale processes and
873 dynamics. In *Ocean modeling in an eddying regime* (p. 17–38). American Geo-
874 physical Union (AGU). doi: 10.1029/177GM04
- 875 Thomas, L. N., Taylor, J. R., Ferrari, R., & Joyce, T. M. (2013). Symmetric in-
876 stability in the Gulf Stream. *Deep Sea Research Part II: Topical Studies in
877 Oceanography*, *91*, 96–110. doi: 10.1016/j.dsr2.2013.02.025
- 878 Thompson, A. F., Lazar, A., Buckingham, C., Naveira Garabato, A. C., Damerell,
879 G. M., & Heywood, K. J. (2016). Open-Ocean Submesoscale Motions: A Full
880 Seasonal Cycle of Mixed Layer Instabilities from Gliders. *Journal of Physical
881 Oceanography*, *46*(4), 1285–1307. doi: 10.1175/JPO-D-15-0170.1
- 882 van Haren, H., Millot, C., & Taupier-Letage, I. (2006). Fast deep sinking in Mediter-
883 ranean eddies. *Geophysical Research Letters*, *33*(4), L04606. doi: 10.1029/
884 2005GL025367
- 885 Waite, A. M., Stemmann, L., Guidi, L., Calil, P. H. R., Hogg, A. M. C., Feng, M.,
886 ... Gorsky, G. (2016). The wineglass effect shapes particle export to the deep
887 ocean in mesoscale eddies. *Geophysical Research Letters*, *43*(18), 9791–9800.
888 doi: 10.1002/2015GL066463
- 889 White, A. E., Letelier, R. M., Whitmire, A. L., Barone, B., Bidigare, R. R., Church,
890 M. J., & Karl, D. M. (2015). Phenology of particle size distributions
891 and primary productivity in the North Pacific subtropical gyre (Station
892 ALOHA). *Journal of Geophysical Research: Oceans*, *120*(11), 7381–7399.
893 doi: 10.1002/2015JC010897